

Article

# Crack Growth in Ni-Cr-Mo-V Steel Using $\Delta$ CTOD Elastic–Plastic Model

Jingxia Yue <sup>1</sup>, Jiankang Lei <sup>1</sup> , Yordan Garbatov <sup>2,\*</sup>  and Ke Yang <sup>3</sup>

<sup>1</sup> School of Naval Architecture, Ocean and Energy Power Engineering, Wuhan University of Technology, Wuhan 430070, China

<sup>2</sup> Centre for Marine Technology and Ocean Engineering (CENTEC), Instituto Superior Técnico, Universidade de Lisboa, 1049-001 Lisbon, Portugal

<sup>3</sup> Wind Power Research and Design Academy, Dongfang Electric Wind Power CO., Ltd., Chengdu 611731, China

\* Correspondence: yordan.garbatov@tecnico.ulisboa.pt

**Abstract:** Many studies have shown that the linear elastic fracture mechanics (LEFM) method based on the stress intensity factor range ( $\Delta K$ ) has limitations that cannot be ignored. Due to neglecting the influence of plastic deformation near the crack tip, LEFM shows apparent deviations in evaluating the fracture behaviour. Therefore, in this study, the crack tip opening displacement range ( $\Delta$ CTOD) is chosen as an alternative to  $\Delta K$  and based on the elastic–plastic fracture mechanics (EPFM) to develop a new fracture behaviour assessment approach for marine structures. Firstly, a  $\Delta$ CTOD model based on the HRR (Hutchinson, Rice, and Rosengren) solution is proposed considering the crack closure effect. Secondly, a series of compact tension (CT) specimen crack growth experiments under constant amplitude loading is carried out. According to the experimental results, the prediction accuracy of the HRR model and traditional Irwin and Dugdale models is compared and analysed. The rationality of  $\Delta$ CTOD as an alternative to  $\Delta K$  is verified. The results show that  $\Delta$ CTOD can describe the crack propagation behaviour well. The proposed HRR model shows better accuracy and a more comprehensive application range than the traditional models, which has a guiding significance for studying fracture behaviour for marine structural applications.

**Keywords:** HRR solution; elastic–plastic fracture mechanics;  $\Delta$ CTOD; crack closure effect; fatigue crack propagation



**Citation:** Yue, J.; Lei, J.; Garbatov, Y.; Yang, K. Crack Growth in Ni-Cr-Mo-V Steel Using  $\Delta$ CTOD Elastic–Plastic Model. *J. Mar. Sci. Eng.* **2022**, *10*, 1944. <https://doi.org/10.3390/jmse10121944>

Academic Editor: Md Jahir Rizvi

Received: 14 November 2022

Accepted: 3 December 2022

Published: 8 December 2022

**Publisher's Note:** MDPI stays neutral with regard to jurisdictional claims in published maps and institutional affiliations.



**Copyright:** © 2022 by the authors. Licensee MDPI, Basel, Switzerland. This article is an open access article distributed under the terms and conditions of the Creative Commons Attribution (CC BY) license (<https://creativecommons.org/licenses/by/4.0/>).

## 1. Introduction

Fatigue failure is considered one of the most severe problems in marine structures during their service life [1]. The extensive use of high-strength steel has increased marine structures' overall deformation and stress levels, resulting in more severe fatigue damage [2,3]. Therefore, it is essential to study the fracture behaviour of high-strength steel materials using the fracture mechanics method to design and reliability assessment of marine structures.

Marine structure design and residual fatigue strength assessment are mainly based on the linear elastic fracture mechanics (LEFM) method. Paris' law [4] established the relationship between the crack propagation rate ( $da/dN$ ) and stress intensity factor range  $\Delta K$ , which significantly contributed to the advance in the understanding of the fracture of different materials and structural components [5]:

$$da/dN = C(\Delta K)^m \quad (1)$$

where  $C$  and  $m$  are material constants obtained from experiments. Ebler [6,7] observed experimentally that the crack closure occurs in the specimen even under tensile load. Since then, many scholars [8–10] have extensively studied the crack closure effect and concluded

that the main driving force controlling the crack propagation should be the effective stress intensity factor amplitude  $\Delta K_{eff}$ , which is defined as:

$$\Delta K_{eff} = K_{max} - K_{po} = U\Delta K \quad (2)$$

where  $K_{max}$  and  $K_{eff}$  are the maximum and the opening stress intensity factor, respectively, and  $U$  is the crack closure coefficient to character crack closure effect.

However, after decades of application, it has been found that there are apparent limitations of the LEFM. Although the effect of the crack tip plastic zone can be neglected for small-scale yielding, the use of fracture parameter  $\Delta K$  leads to significant deviations in the predicted crack propagation rate when large-scale plastic deformation occurs at the crack tip. For this reason, two fracture parameters,  $J$ -integral and crack tip opening displacement ( $CTOD$ ), were introduced to replace the stress intensity factor  $K$ .

Rice [11] and Cherepanov [12] proposed a concept of the path-independent  $J$ -integral, and Hutchinson [13], Rice, and Rosengren [14] established the HRR singular field theory. The HRR solution describes the elastic–plastic stress–strain distribution at the crack tip of the power-law hardening materials, and the  $J$ -integral characterizes the strength of the HRR singular field. Some studies focused on the HRR field characterized by  $J$ -integral. Shih et al. [15,16] calculated the angular distribution function of the HRR solution through the finite element method (FEM) and summarized it into a table, which greatly facilitated the use of the HRR solution. Homayoun et al. [17] calculated the stress–strain field at the mode I crack tip using the HRR solution, linear elastic FEM, and elastic–plastic FEM. The HRR solution results were closer to those of the elastic–plastic FEM solution, indicating that the HRR solution is suitable for solving the elastic–plastic fracture problem.

Zou et al. [18] analyzed the axial and radial stress distributions near the crack tip through FEM, which was in good agreement with the HRR solution, indicating that the HRR solution can reflect the stress–strain distribution at the crack tip accurately. However, since the  $J$ -integral is path-independent only when the assumption of total plastic deformation is satisfied, the HRR solution only applies to monotonic loading processes [19].

The concept of  $CTOD$  was proposed by Wells [20] based on the number of tests, which has clear physical significance and can be directly measured during the tests. One of the basic mechanisms for fatigue crack propagation is based on the crack-tip blunting under maximum load and the re-sharpening of the crack-tip under minimum load [21–24]. Antunes et al. [23] used numerical methods to calculate  $CTOD$  for two aluminium alloy middle tension (MT) specimens, Krzysztof [25] presented fatigue crack propagation rate and  $CTOD$  for high-strength steel under tensile loading, and Vasco-Olmo and James [26] proposed a method to measure and analyze  $CTOD$  from experimental data. These studies indicate that  $CTOD$  can be a viable alternative to  $\Delta K$  for characterizing fatigue crack expansion.

There are two main numerical models commonly used to estimate  $CTOD$ . One is the Irwin model, which is derived based on the modified plastic zone size as proposed in [27] for the linear elastic fracture problem, and therefore it is only applicable to the case of small-scale yielding. The other is the Dugdale model [28], which treats the crack-tip plastic zone as a flat ribbon and uses the superposition principle to transform the complex elastic–plastic problem into two simple linear-elastic problems, thus achieving the solution of  $CTOD$  for the large-scale yielding condition.

However, the accuracy and applicability of the Dugdale model are questionable because it ignores the effect of material hardening and incorrectly assumes the shape of the plastic zone at the crack tip [29,30].

The HRR solution can accurately describe the elastic–plastic stress–strain field of the crack tip, but it is unsuitable for cyclic loading.  $CTOD$  can characterize the crack propagation behaviour under cyclic loading, but there is no accurate numerical solution. Therefore, the following work is carried out to characterize the crack propagation behaviour under cyclic loading. Firstly, the plastic zone size of the crack tip is deduced based on the HRR solution, which characterizes the crack tip's elastic–plastic stress and strain field. The  $\Delta CTOD$  numerical model (HRR model) is further proposed considering the crack closure

effect. Section 3 introduces the CT specimen size, experimental device, and measurement method. According to the established loading conditions, a series of crack propagation experiments of CT specimens made of Ni-Cr-Mo-V high-strength steel used in naval ship construction are carried out. Section 4 compares the accuracy and applicability of the Irwin, Dugdale, and HRR models proposed in this study analyses them based on the experimental results. All the conclusions of this study are summarized lastly.

## 2. Numerical Methods

Fracture mechanics [31] defines the  $J$ -integral of the two-dimensional (2D) planar crack as follows:

$$J = \int_{\Gamma} [Wdy - T_i \frac{\partial u_i}{\partial x} ds] \tag{3}$$

where  $\Gamma$  is the integration contour pointing from the lower crack surface to the upper crack surface;  $W$  is the strain energy density;  $\sigma_{ij}$ ,  $\epsilon_{ij}$ , and  $u_i$  are the stress, strain, and displacement fields near the crack tip, respectively;  $T_i$  is the tension vector on the crack body bounded by  $\Gamma$ ; and  $ds$  is the differential element along the contour  $\Gamma$ :

$$W = \sigma_{ji}\epsilon_{ji} \tag{4}$$

Since the above-defined equation is inconvenient to use in engineering, the  $J$ -integral was divided into the elastic component  $J_e$  and plastic component  $J_p$ :

$$J = J_e + J_p \tag{5}$$

For the CT specimen, the relationship between  $J_e$  and the stress intensity factor (SIF) is defined as:

$$J_e = \frac{K^2}{E} \tag{6}$$

while the SIF can be determined by [32]:

$$K = \frac{P}{B\sqrt{W}} \frac{(2 + \beta)}{(1 - \beta)^{3/2}} (0.886 + 4.64\beta - 13.32\beta^2 + 14.72\beta^3 - 5.6\beta^4) \tag{7}$$

where  $P$  is the far-field load,  $B$  and  $W$  are the thickness and width, respectively, of the CT specimen, and  $\beta = a/W$  is the shape factor of the CT specimen.  $a$  is the crack length of the CT specimen.

The  $J$ -integral plastic component  $J_p$  of the CT specimen can be calculated employing engineering estimation as:

$$J_p = \alpha \sigma_{ys} \epsilon_{ys} c h_1(a/W, n) (P/P_0)^{n+1} \tag{8}$$

where  $\alpha$  and  $n$  are the hardening coefficient and index of the material, respectively, and  $\sigma_{ys}$  and  $\epsilon_{ys}$  are the material's yield stress and strain, respectively.  $c$  is the remaining ligament length of the CT specimen,  $h_1(a/W, n)$  is a function related to  $a/W$  and  $n$  only, and the values can be found in reference [33].  $P_0$  is the ultimate load per unit thickness of the specimen and is given by:

$$P_0 = 1.071 \left\{ \left[ \left( \frac{2a}{c} \right)^2 + 2 \left( \frac{2a}{c} \right) + 2 \right]^{1/2} - \left[ \left( \frac{2a}{c} \right) + 1 \right] \right\} c \sigma_{ys} \tag{9}$$

A plastic zone's presence leads to crack tip blunting [34]. To estimate the crack's plastic zone size, a numerical model of CTOD is established.

In the LEFM, the longitudinal stress  $\sigma_y$ , which is perpendicular to the crack propagation direction, can be calculated as [35]:

$$\sigma_y = \frac{K_I}{\sqrt{2\pi r}} \tag{10}$$

where  $K_I$  is the SIF of the mode I crack and  $r$  is the distance along the extended line of the crack from the crack tip. To explain the phenomenon of small-scale yielding near the crack tip in LEFM, Irwin [27] proposed that the plastic zone size can be determined by assuming  $\sigma_y = \sigma_{ys}$ . Therefore, the plastic zone size  $r_p$  of mode I crack is as follows:

$$r_p = \frac{\sigma^2 a}{2\sigma_{ys}^2} = \frac{K_I^2}{2\pi\sigma_{ys}^2} \tag{11}$$

Dugdale regarded the plastic zone size of the crack tip as a narrow strip and assumed that the upper and lower surfaces of the plastic zone carry the compressive stresses equal to yield stress  $\sigma_{ys}$  uniformly.

According to the condition that there is no stress singularity near the crack tip ( $K_I = 0$ ),  $K_\sigma$  caused by the far-field stress  $\sigma$  should be offset by  $K_\rho$  caused by the compressive stress  $\sigma_{ys}$  acting on the crack surface:

$$K_\sigma = -K_\rho \tag{12}$$

The equations of  $K_\sigma$  and  $K_\rho$  can be taken into account to obtain the following:

$$\sigma\sqrt{\pi(a + \rho)} = 2\sigma_{ys}\sqrt{\frac{a + \rho}{\pi}}\arccos\frac{a}{a + \rho} \tag{13}$$

The plastic zone size of the crack tip can be deduced based on Dugdale’s method:

$$r_p = \frac{\pi^2\sigma^2 a}{8\sigma_{ys}^2} \tag{14}$$

Based on the HRR solution, the elastic–plastic stress field of the mode I crack can be calculated as follows:

$$\sigma_{ij}(r, \theta) = \sigma_{ys}\left(\frac{EJ}{\alpha\sigma_{ys}^2 I_n r}\right)^{1/n+1} \tilde{\sigma}_{ij}(\theta, n) \tag{15}$$

where  $r$  and  $\theta$  are the polar coordinates at the crack tip.  $I_n$  is an integration constant related to hardening index  $n$  only,  $\tilde{\sigma}_{ij}(\theta, n)$  do  $n$  and  $\theta$  determine the angular momentum function. The values of  $I_n$  and  $\tilde{\sigma}_{ij}(\theta, n)$  can be found in reference [15].

When  $\theta = 0^\circ$ , the  $\sigma_y$  can be estimated as:

$$\sigma_y = \sigma_{\theta\theta} = \sigma_{ys}\left(\frac{EJ}{\alpha\sigma_{ys}^2 I_n r}\right)^{1/n+1} \tilde{\sigma}_{\theta\theta}(\theta, n) \tag{16}$$

When  $\sigma_y = \sigma_{ys}$ , the plastic zone size of the crack tip is defined as:

$$r_p = \frac{EJ[\tilde{\sigma}_{\theta\theta}(\theta, n)]^{n+1}}{\alpha\sigma_{ys}^2 I_n} \tag{17}$$

For the crack body, the relationship between CTOD and  $r_p$  is as follows [36]:

$$CTOD = \frac{4\sigma}{E}\sqrt{2ar_p + (r_p)^2} \tag{18}$$

Considering the crack closure effect, the crack tip opening displacement range  $\Delta CTOD$  can be calculated as:

$$\Delta CTOD = CTOD_{max} - CTOD_{min} = \frac{4\Delta\sigma_{eff}}{E} \sqrt{2ar_p + (r_p)^2} \tag{19}$$

where  $\Delta CTOD$  is the crack tip opening displacement range;  $CTOD_{max}$  and  $CTOD_{min}$  are the maximum and minimum opening displacement, respectively; and  $\Delta\sigma_{eff}$  is the effective far-field stress range, which is defined as:

$$\Delta\sigma_{eff} = U\Delta\sigma = U(\sigma_{max} - \sigma_{min}) \tag{20}$$

where  $\Delta\sigma$ ,  $\sigma_{max}$ , and  $\sigma_{min}$  are the far-field stress range and maximum and minimum far-field stress, respectively;  $U$  is the coefficient reflecting the crack closure effect, which is defined as:

$$U = \frac{\sigma_{max} - \sigma_{op}}{\sigma_{max} - \sigma_{min}} = \frac{P_{max} - P_{op}}{P_{max} - P_{min}} \tag{21}$$

where  $P_{max}$  and  $P_{min}$  are the maximum and minimum far-field loading, respectively;  $\sigma_{op}$  and  $P_{op}$  represent the stress and loading associated with the crack opening.

Based on the formula of plastic zone sizes, three numerical models of  $\Delta CTOD$  can be calculated as follows:

$$\Delta CTOD = \frac{4U^2\Delta K^2}{\pi E\sigma_{ys}} = \frac{4aU^2\Delta\sigma^2}{E\sigma_{ys}} \text{ (Irwin model)} \tag{22}$$

$$\Delta CTOD = \frac{2U^2\Delta K^2}{E\sigma_{ys}} = \frac{2\pi aU^2\Delta\sigma^2}{E\sigma_{ys}} \text{ (Dugdale model)} \tag{23}$$

$$\Delta CTOD = \frac{4U\Delta\sigma\Delta J[\tilde{\sigma}_{\theta\theta}(\theta, n)]^{n+1}}{\alpha\sigma_{ys}^2 I_n} \sqrt{1 + \frac{2\alpha\alpha\sigma_{ys}^2 I_n}{E\Delta J[\tilde{\sigma}_{\theta\theta}(\theta, n)]^{n+1}}} \text{ (HRR model)} \tag{24}$$

It should be noted that both the Irwin and Dugdale models neglect  $(r_p)^2$  in the estimation of  $\Delta CTOD$  due to the assumption that the plastic zone size  $r_p$  is much smaller than the crack length  $a$ .

### 3. Experimental Analysis

#### 3.1. Specimen Characteristics

CT specimens were prepared to verify the above  $CTOD$  numerical models, and a series of crack propagation experiments were performed according to ASTM E647 [32]. It should be noted that in the investigation, CT specimens are designed and manufactured according to the plane stress state to characterize the crack propagation behaviour of the hull deck and shell plates. The plane strain state has not been discussed. All specimens were machined from the same steel plate with an original plate thickness of 12 mm. The machining process of CT specimens was controlled in the L-T direction to ensure different specimens had similar fatigue performance. The machined notch of the CT specimen was made via electrical discharge machining (EDM), while the 4 mm pre-cracks were cut by 0.02 mm molybdenum wire. The degree of finish at the surface of the CT specimen was polished to 0.8  $\mu\text{m}$  by an electric sander, which ensures that the surface texture was perpendicular to the crack propagation direction for crack observation easier. The configuration of the CT specimen is shown in Figure 1.

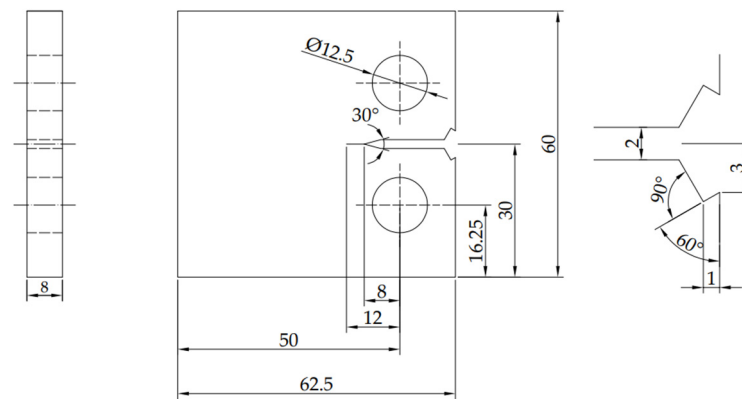


**Figure 1.** Configuration of CT specimen.

The material used for the CT specimen is Ni-Cr-Mo-V high-strength steel. To determine the parameters of the Ramberg–Osgood model is used in the HRR solution:

$$\varepsilon = \frac{\sigma}{E} + \alpha \varepsilon_{ys} \left( \frac{\sigma}{\sigma_{ys}} \right)^n \quad (25)$$

Uniaxial tensile tests of the Ni-Cr-Mo-V high-strength steel were carried out at room temperature to obtain the mechanical properties, as shown in Table 1.

**Table 1.** Material mechanical properties of Ni-Cr-Mo-V high-strength steel at room temperature.

Mechanical Property	Unit	Value
Density ( $\rho$ )	kg/m <sup>3</sup>	7850
Modulus of elasticity ( $E$ )	GPa	219
Poisson’s ratio ( $\nu$ )	-	0.35
Yield strength ( $\sigma_{ys}$ )	MPa	635
Ultimate strength ( $\sigma_u$ )	MPa	680
Hardening coefficient ( $\alpha$ )	-	0.11
Hardening index ( $n$ )	-	4.237

### 3.2. Test Setup

All CT specimens were tested on the MTS322 fatigue test machine with a load capacity of 200 kN at room temperature. The fracture mechanics clevis grip was used for specimen clamping and fixing. The crack propagation experiments of CT specimens were carried out under sine wave load control conditions. A loading frequency that is too high may distort the applied load, so the loading frequency was set to 10 Hz in this experiment to achieve a loading accuracy of 0.01 kN.

Loading conditions under different load amplitudes and load ratios were set to verify the applicability of different numerical models, as shown in Table 2.

**Table 2.** Crack propagation experiment loading conditions of CT specimens.

Specimen	$P_a$ <sup>1*</sup> (kN)	$R$ <sup>2*</sup>	$P_m$ <sup>3*</sup> (kN)
CT01	2.70	0.1	3.30
CT02	3.60	0.1	4.40
CT03	4.50	0.1	5.50
CT04	3.60	−0.1	2.95
CT05	3.60	0.3	6.69
CT06	3.60	0.7	20.40

<sup>1\*</sup> load amplitude, <sup>2\*</sup> load ratio, <sup>3\*</sup> mean load.

The CT specimens were observed for crack length and *CTOD* using a CCD microscope camera combined with the digital image correlation (DIC) analysis software VIC-2D. The CCD camera was positioned perpendicular to the surface of the CT specimen, and the magnification was adjusted to provide clear optical images of the crack propagation area in real time. Before the experiment, all CT specimens were sprayed with a speckle pattern and calibrated with a transparent scale to facilitate subsequent image processing. In addition, a high-sensitivity strain gauge was attached to the back of the CT specimen to measure back strain for estimating crack opening force  $P_{op}$ . The general arrangement of the test setup is shown in Figure 2, and the detail of the CT specimen is shown in Figure 3.

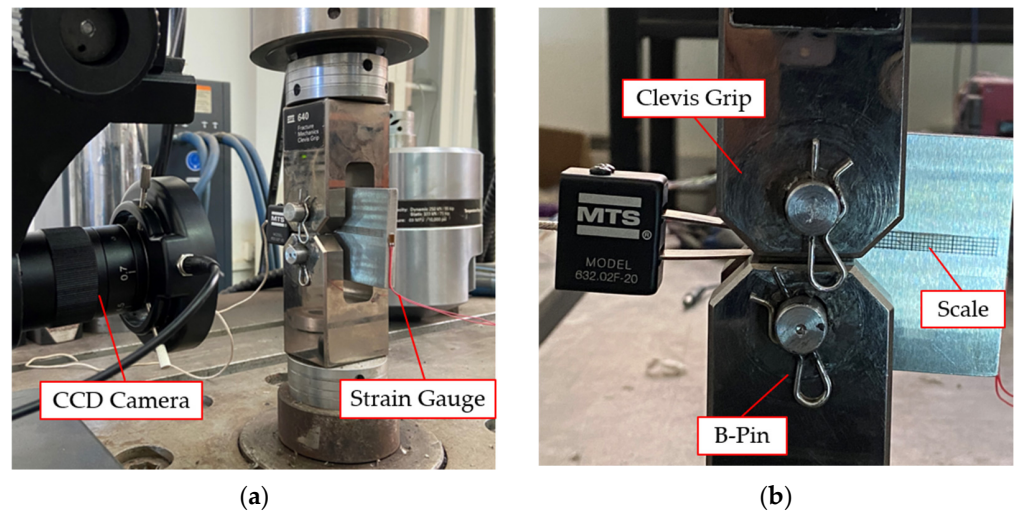


Figure 2. Measurement system: (a) global; (b) local.

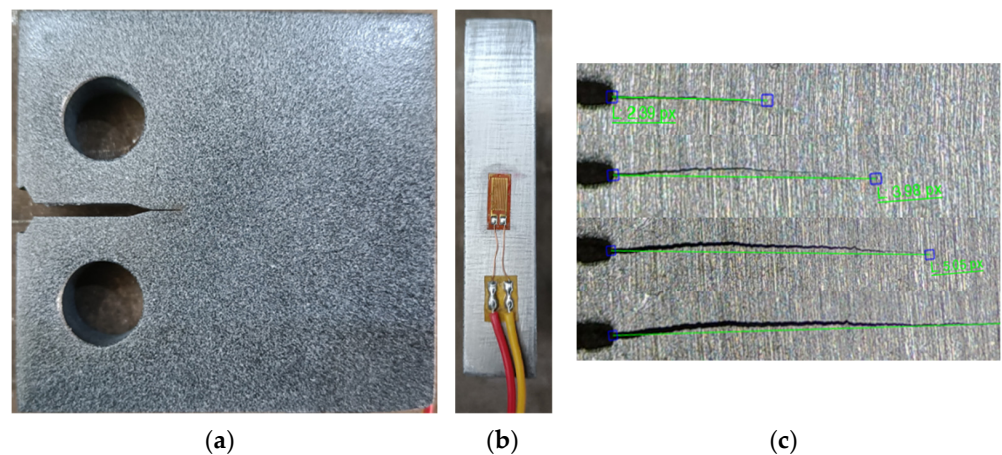


Figure 3. CT specimen: (a) speckle pattern, (b) back strain gauge, (c) crack observation.

The experiment measured the *CTOD* and back strain in approximately 2 mm crack increments. To obtain sufficient images for DIC analysis, the loading frequency was decreased to 0.1 Hz, and the sampling frequency was set to 50 Hz, which enabled 500 images to be captured within one load cycle. The time history data of the loading force was recorded by the software system of the MTS test machine, and the sampling frequency was set to 500 Hz.

### 3.3. Digital Image Correlation

The principle of the DIC technique is to match the maximum correlation between a subset of sample images at different deformation stages and to obtain the displacement and strain fields of the specimen by estimating the correlation changes of the grayscale

information of the specimen surface images [37,38]. DIC is a non-contact full-field measurement technique able to obtain the total (elastic plus plastic) strain on the surface of the specimen. Therefore, the elastic and plastic components can all be measured using DIC [23,39]. The DIC technique is applied to measure the crack length and  $\Delta CTOD$ , as shown in Figure 4, where the “Inspect line” parallel to the crack propagation direction and the “Virtual extensometer” perpendicular to the crack propagation direction are added in the image analysis area.

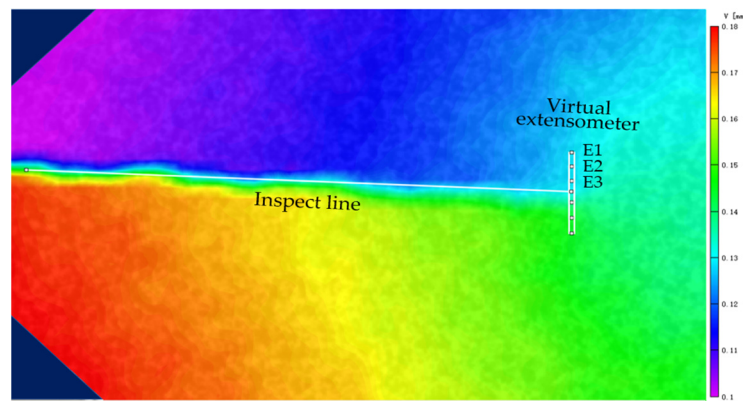


Figure 4. Crack length and  $\Delta CTOD$  measurement via the DIC technique.

The “Inspect line” length corresponds to the crack length of the specimen, and the displacement deformation of the “Virtual extensometer” corresponds to the  $CTOD$  of the specimen. Therefore, the  $\Delta CTOD$  can be calculated as:

$$\Delta CTOD = L_{max} - L_{min} \tag{26}$$

where  $L_{max}$  and  $L_{min}$  are the maximum and minimum lengths of the “Virtual extensometer” in a loading cycle.

Additionally, to ensure the validity of measured results, three virtual extensometers (E1, E2, E3) with different ranges are added to investigate the effect of the extensometer range. As can be seen from Figure 5, there are slight differences in the measurement results of different extensometers, but such differences can be ignored when the extensometer range is small enough. In this study, measurement results of the E3 extensometer are taken as the final experimental data.

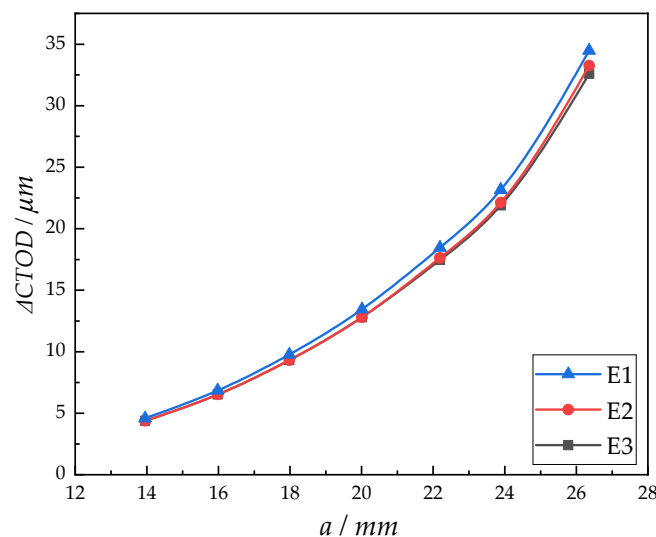


Figure 5. Measurement results with different ranges of extensometers (CT06).

### 4. Results and Discussion

#### 4.1. Crack Closure Coefficient $U$

Based on the strain-loading force ( $\epsilon$ - $P$ ) curve obtained from the experiment, the crack opening force  $P_{op}$  was determined using the compliance offset method in ASTM E647. The compliance offset value should be set at 1%, 2%, and 4%, and the specific value depends on the data dispersion of the compliance offset curve measured in the experiment.

As shown in Figure 6, a unique corresponding crack opening force can be obtained by setting the compliance offset value as 4%. The calculated  $P_{op}$  for each loading condition is shown in Figure 7.

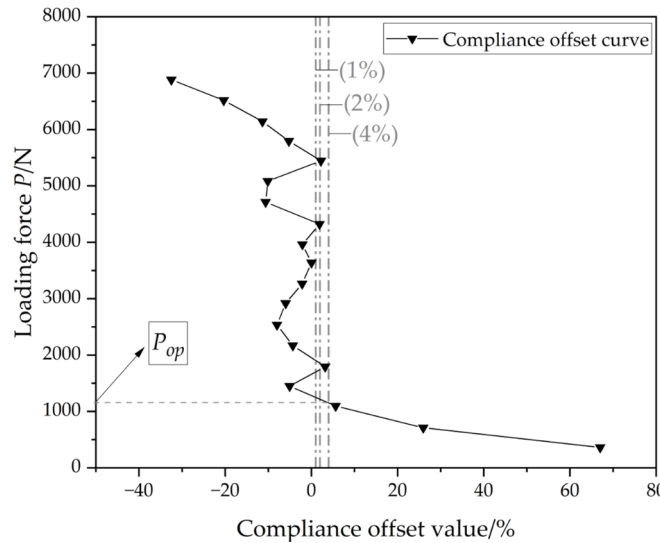


Figure 6. Loading force versus compliance offset value curve of CT01.

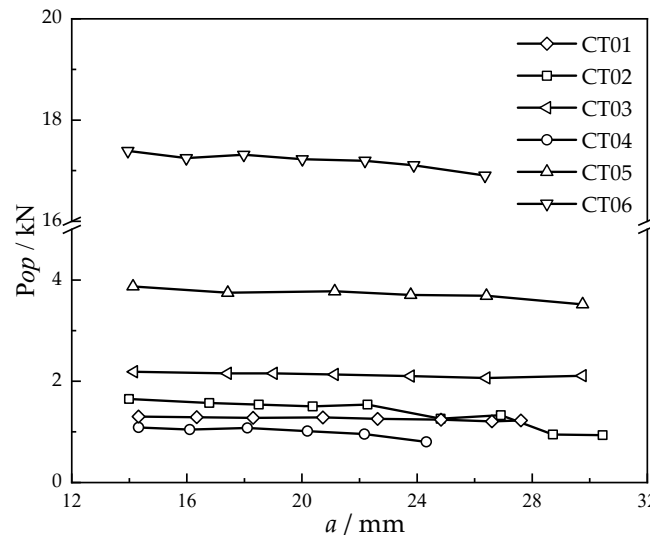


Figure 7. Crack opening force of CT specimens under different loading conditions.

From Figure 7,  $P_{op}$  shows a decreasing trend as the crack length increases, indicating that the closure effect decreases with the crack length increase, but the degree of decrease is fragile. The study presented in [40] also points out that  $P_{op}$  generally decreases with increasing the crack length near the threshold, while in the sound propagation stage, the decreasing trend of  $P_{op}$  will slow down until stable.

In addition, the crack closure coefficient  $U$  for all loading conditions was calculated based on the crack opening force data obtained from the experiment and summarized in

Table 3. From Table 3, the crack closure coefficient increases significantly with the increase in load ratio (CT02, CT04, CT05, CT06) but is hardly affected by the load amplitude (CT01, CT02, CT03), so it can be assumed that the crack closure coefficient  $U$  is only related to the load ratio  $R$  and the  $U$ - $R$  fitted rule is obtained accordingly:

$$U = 0.57R^3 - 0.93R^2 + 0.53R + 0.83 \quad (-0.1 \leq R \leq 0.7) \quad (27)$$

Table 3. The crack opening force and crack closure coefficient under different loading conditions.

Specimen	$P_a$ (kN)	$R$	$P_{op}$ (kN)	$U$
CT01	2.70	0.1	1.26	0.878
CT02	3.60	0.1	1.65	0.882
CT03	4.50	0.1	2.13	0.874
CT04	3.60	-0.1	1.05	0.764
CT05	3.60	0.3	3.71	0.914
CT06	3.60	0.7	17.20	0.945

#### 4.2. $da/dN$ - $\Delta CTOD$ Curve

The crack lengths and  $\Delta CTOD$  of the CT specimens under all loading conditions were measured using the DIC technique, and the  $da/dN$ - $\Delta CTOD$  curves shown in Figure 8 were plotted in combination with loading cycles recorded by the fatigue test machine. As shown in Figure 8, the crack propagation rate shows a linear correlation with  $\Delta CTOD$  similar to Paris' law in the double logarithmic coordinate system, which indicates that  $\Delta CTOD$  can be used to describe the crack propagation rate instead of  $\Delta K$ . The fitted crack propagation rate model was obtained as follows:

$$da/dN = 8.135 \times 10^{-3} (\Delta CTOD)^{0.839} \quad (28)$$

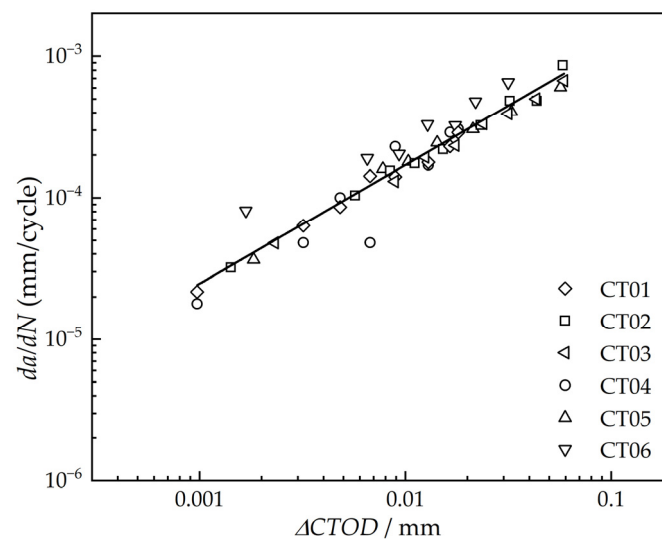


Figure 8. Crack propagation rate  $da/dN$  versus  $\Delta CTOD$  curve.

#### 4.3. Comparison

The  $a$ - $\Delta CTOD$  curves obtained from the numerical models and crack propagation experiments under all loading conditions are summarized in Figure 9. With the increase in crack length, the trend of  $\Delta CTOD$  experimental value is almost the same as the numerical prediction curve. It only slows down at the early and late stages of crack propagation. There are two main reasons for this phenomenon. EDM machined the notch and pre-crack of the CT specimen, and residual compressive stresses inevitably affected the vicinity of the pre-crack. Therefore, in the early stage of the crack propagation, residual compressive

stresses increase the difficulty of the crack opening, leading to minor  $\Delta CTOD$  experimental results than numerically predicted results. This phenomenon disappears gradually with the increase in loading cycles. The higher the applied load, the faster it disappears, as verified by the experimental results of CT01, CT02, and CT03 specimens in Figure 9.

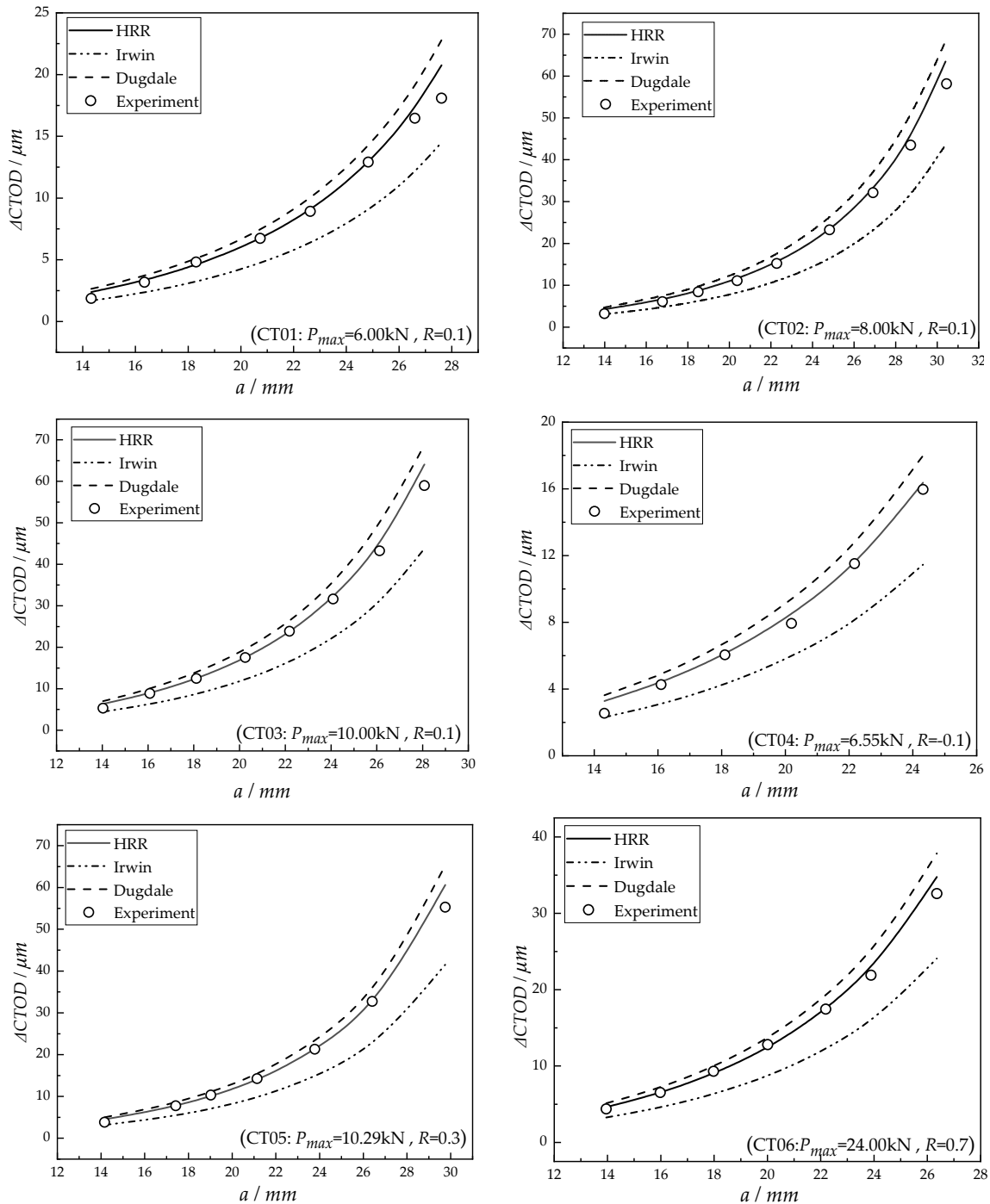


Figure 9. Numerical and experimental  $a$ - $da/dN$  curve under all loading conditions.

The CT specimen is loaded and fixed through the pin connection. With the continuous action of applied load, the contact position between the specimen and the pin will be deformed. The deformation will weaken the restraint effect of the pin on the CT specimen, resulting in more minor experimental results. This phenomenon occurs earlier when

the applied load is higher, verified by the experimental results of CT02, CT05, and CT06 specimens in Figure 9.

For the above reasons, the first and last experimental data points for all loading conditions were excluded when comparing the prediction accuracy of the three numerical models. To evaluate the prediction ability of three numerical models, two error rating indicators,  $E_a$  and  $E_{max}$ , are calculated and summarized in Table 4.  $E_a$  and  $E_{max}$  are the mean and maximum absolute error of predicted results compared to experimental data, respectively, which are calculated as follows:

$$E_a = \frac{1}{n} \sum_{i=1}^n \left| \left( \frac{t_{mi} - t_{ei}}{t_{ei}} \right) \times 100\% \right| \tag{29}$$

$$E_{max} = \max \left\{ \left| \left( \frac{t_{mi} - t_{ei}}{t_{ei}} \right) \times 100\% \right| \right\} \quad (i = 1, 2, \dots, n) \tag{30}$$

where  $t_{mi}$  is the prediction result of the model, and  $t_{ei}$  is the experimental result.

**Table 4.** Error statistics of numerical model prediction results.

Model	Error Index	CT01	CT02	CT03	CT04	CT05	CT06
Irwin	$E_a$	28.55%	28.47%	29.35%	28.01%	30.31%	29.77%
	$E_{max}$	32.50%	30.58%	30.59%	29.25%	31.47%	31.66%
Dugdale	$E_a$	12.24%	12.37%	10.98%	13.08%	9.47%	10.32%
	$E_{max}$	17.04%	16.85%	13.46%	15.00%	11.03%	15.37%
HRR	$E_a$	3.05%	2.58%	1.59%	2.42%	1.14%	2.34%
	$E_{max}$	5.77%	5.82%	4.85%	3.98%	2.31%	5.40%

According to Figure 9 and Table 4, the  $a$ - $\Delta$ CTOD prediction curve of the Irwin model lies below the experimental data overall, the mean error of the Irwin model is more than 25%, and the maximum error reaches about 30%. On the contrary, the  $a$ - $\Delta$ CTOD prediction curve of the Dugdale model lies above the experimental data overall, the mean error of the Dugdale model stays within 15%, and the maximum error is less than 20%. In addition, it can be seen that the Dugdale model has good accuracy at the early stage of crack propagation. Still, the accuracy decreases gradually with increased crack length or applied load. While the  $a$ - $\Delta$ CTOD prediction curve of the HRR model agrees well with the experimental data, the mean error of the HRR model is kept within 4%, and the maximum error is around 6%.

The reasons for the above phenomenon can be explained by the fact that the Irwin model is based on small-scale yielding, which assumes that the plastic zone size is much smaller than the crack size. This assumption causes the prediction accuracy of the Irwin model to decrease as the crack length or applied load increases, as verified by the error data for CT02, CT04, CT05, and CT06 in Table 4.

The Dugdale model ignores the effect of material hardening parameters, and the hardening effect of material will lead to plastic energy dissipation during crack propagation [41,42]. The increase in the crack length or applied load leads to an increase in the plastic zone size of the crack tip, which intensifies the plastic energy dissipation and thus leads to a more significant prediction error of the Dugdale model.

The HRR model was established based on  $J$ -integral. It considers the material hardening effect, concluding that the HRR model can accurately describe the crack tip elastic–plastic stress–strain field. Its predictions are more accurate than the Irwin and Dugdale models at the significant loadings.

### 5. Conclusions

A newly developed model based on the HRR considering the elastic–plastic stress–strain field at the crack tip of mode I crack and crack closure effect applies to  $\Delta$ CTOD under

constant amplitude loading. A series of crack propagation experiments on CT specimens made of Ni-Cr-Mo-V high-strength steel was conducted to verify the applicability of  $\Delta CTOD$  to describe the crack propagation behaviour. Additionally, the accuracy of the HRR model proposed in this study was compared to the traditional methods (Irwin and Dugdale models) based on the experimental results.

Several conclusions are drawn from the present study.

- According to the crack opening force results from experiments, the crack closure coefficient  $U$  is almost independent of the load amplitude  $P_a$  and only related to the loading ratio  $R$ . Based on this phenomenon, the equation for  $U$  was provided.
- In the double logarithmic coordinate system, there is a linear correlation between the crack propagation rate  $da/dN$  and  $\Delta CTOD$  that is like Paris' law, which indicates that  $\Delta CTOD$  is a feasible alternative to  $\Delta K$ .
- The Irwin model assumes small-scale yielding, which considers the plastic zone size much smaller than the crack size, thus tends to underestimate the value of  $\Delta CTOD$  with a significant error and is not recommended for the prediction of  $\Delta CTOD$  in elastic–plastic fracture problems.
- The Dugdale model has good predictability when the crack length or applied load is small. However, since the Dugdale model ignores the effect of material hardening, it tends to overestimate  $\Delta CTOD$  and the error increases with the crack length or applied load. Therefore, the applicability range should be verified using the Dugdale model for  $\Delta CTOD$  prediction.
- Since the material hardening effect is considered, the HRR model is more accurate in describing the elastic–plastic stress–strain field at the crack tip of the CT specimen than the Irwin and Dugdale models. Thus, the  $\Delta CTOD$  is better-predicted. Therefore, the HRR model proposed in the present study is recommended for predicting  $\Delta CTOD$  in elastic–plastic fracture mechanics problems.

**Author Contributions:** Writing—original draft preparation, J.L., J.Y. and K.Y.; writing—review and editing, J.Y. and Y.G. All authors have read and agreed to the published version of the manuscript.

**Funding:** This research was funded by the National Natural Science Foundation of China (No. 52171320).

**Institutional Review Board Statement:** Not applicable.

**Informed Consent Statement:** Not applicable.

**Data Availability Statement:** The data presented in this study are available on request from the corresponding author.

**Conflicts of Interest:** The authors declare no conflict of interest.

## References

1. Yue, J.; Dang, Z.; Guedes Soares, C. Prediction of fatigue crack propagation in bulb stiffeners by experimental and numerical methods. *Int. J. Fatigue* **2017**, *99*, 101–110. [[CrossRef](#)]
2. Lei, J.; Yue, J.; Xu, Z.; Fang, X.; Liu, H. Theoretical and Experimental Analysis on Low-Cycle Fatigue Crack Initiation for High Strength Steel Stiffened Plates. In Proceedings of the ASME 2022 41st International Conference on Ocean, Offshore and Arctic Engineering, Hamburg, Germany, 5–10 June 2022.
3. Tu, W.; Yue, J.; Xie, H.; Tang, W. Fatigue Crack Propagation Behavior of High-strength Steel under Variable Amplitude Loading. *Eng. Fract. Mech.* **2021**, *247*, 107642. [[CrossRef](#)]
4. Paris, P. A critical analysis of crack propagation laws. *J. Basic Eng.* **1963**, *85*, 528–533. [[CrossRef](#)]
5. Hagihara, S.; Shishido, N.; Hayama, Y.; Miyazaki, N. Methodology for calculating J-integral range  $\Delta J$  under cyclic loading. *Int. J. Press. Vessel. Pip.* **2021**, *191*, 104343. [[CrossRef](#)]
6. Elber, W. Fatigue crack closure under cyclic tension. *Eng. Fract. Mech.* **1970**, *2*, 37–45.
7. Elber, W. The Significance of Fatigue Crack Closure. *ASTM STP* **1971**, *486*, 230–242.
8. Codrington, J.; Kotousov, A. A crack closure model of fatigue crack growth in plates of finite thickness under small-scale yielding conditions. *Mech. Mater.* **2009**, *41*, 165–173. [[CrossRef](#)]

9. Antunes, F.V.; Rodrigues, D.M.; Branco, R. An analytical model of plasticity-induced crack closure. *Procedia Eng.* **2010**, *2*, 1005–1014. [[CrossRef](#)]
10. Ould Chikh, B.; Imad, A.; Meddah, H.M.; Bouchouicha, B.; Benguediab, M. An experimental study of loading parameters effect on fatigue crack closure in 12NC6 steel(Article). *Mech. Mater.* **2012**, *46*, 83–93. [[CrossRef](#)]
11. Rice, J.R. A path independent integral and the approximate analysis of strain concentration by notches and cracks. *J. Appl. Mech.* **1968**, *35*, 379–386. [[CrossRef](#)]
12. Cherepanov, G.P.; Becher, P.; Freiman, S. On crack propagation in solids. *Int. J. Solids Struct* **1969**, *5*, 863–871.
13. Hutchinson, J.W. Singular behaviour at the end of a tensile crack in a hardening material. *J. Mech. Phys. Solids* **1968**, *16*, 13–31. [[CrossRef](#)]
14. Rice, J.R.; Rosengren, G.F. Plane strain deformation near a crack tip in a power-law hardening material. *J. Mech. Phys. Solids* **1968**, *16*, 1–12. [[CrossRef](#)]
15. Shih, C. *Tables of HRR Singular Field Quantities*; MRL E-147; Division of Engineering, Brown University: Providence, RI, USA, 1983.
16. Shih, C.; German, M. Requirements for a one-parameter characterization of crack tip fields by the HRR singularity. *Int. J. Fract.* **1981**, *17*, 27–43. [[CrossRef](#)]
17. Alizadeh, H.; Bedare, A.R.; Bhat, S. Finite Element Examination and Validation of Stress Field around Ductile Mode I Crack Tip in Elastic-Plastic Fracture. In *Advanced Materials Research*; Trans Tech Publications Ltd.: Wollerau, Switzerland, 2013; pp. 342–347.
18. Zou, J.; Jing, H.; Xu, L. Surface crack fracture toughness and HRR fields of ultra-high strength steel. *J. Mater. Sci. Eng. A* **2007**, *454*, 467–471. [[CrossRef](#)]
19. Xu, M.; Liu, Y.; Yuan, H. On  $\Delta J$  characterization of elastic-plastic crack-tip fields under fatigue loading conditions. *Int. J. Fatigue* **2022**, *160*, 106849. [[CrossRef](#)]
20. Wells, A.A. Unstable crack propagation in metals: Cleavage and fast fracture. In *Proceedings of the Crack Propagation Symposium*, Cranfield, UK; 1961.
21. Laird, C.; Smith, G.C. Crack propagation in high stress fatigue. *Philos. Mag.* **1962**, *7*, 847–857. [[CrossRef](#)]
22. Hunnell, J.M.; Kujawski, D. Numerical simulation of fatigue crack growth behaviour by crack-tip blunting. *Eng. Fract. Mech.* **2009**, *76*, 2056–2064. [[CrossRef](#)]
23. Antunes, F.V.; Rodrigues, S.M.; Branco, R.; Camas, D. A numerical analysis of CTOD in constant amplitude fatigue crack growth. *Theor. Appl. Fract. Mech.* **2016**, *85*, 45–55. [[CrossRef](#)]
24. Dong, Q.; Yang, P.; Xu, G. Low cycle fatigue analysis of CTOD under variable amplitude loading for AH-32 steel. *Mar. Struct.* **2019**, *63*, 257–268. [[CrossRef](#)]
25. Werner, K. The fatigue crack growth rate and crack opening displacement in 18G2A-steel under tension. *Int. J. Fatigue* **2012**, *39*, 25–31. [[CrossRef](#)]
26. Vasco-Olmo, J.M.; Díaz, F.A.; Antunes, F.V.; James, M.N. Experimental evaluation of CTOD in constant amplitude fatigue crack growth from crack tip displacement fields. *Frat. Integrità Strutt.* **2017**, *11*, 157–165. [[CrossRef](#)]
27. Irwin, G. Linear fracture mechanics, fracture transition, and fracture control. *Eng. Fract. Mech.* **1968**, *1*, 241–257. [[CrossRef](#)]
28. Dugdale, D.S. Yielding of steel sheets containing slits. *J. Mech. Phys. Solids* **1960**, *8*, 100–104. [[CrossRef](#)]
29. Chen, J.; Huang, Y.; Dong, L.; Li, Y. A new method for cyclic crack-tip plastic zone size determination under cyclic tensile load. *Eng. Fract. Mech.* **2014**, *126*, 141–154.
30. Neimitz, A. Modification of Dugdale model to include the work hardening and in-and out-of-plane constraints. *Eng. Fract. Mech.* **2004**, *71*, 1585–1600. [[CrossRef](#)]
31. Perez, N. Fatigue Crack Growth. In *Fracture Mechanics*; Springer International Publishing: Cham, Switzerland, 2017; pp. 327–372.
32. ASTM. *Standard Test Method for Measurement of Fatigue Crack Growth Rates*; ASTM International: West Conshohocken, PA, USA, 2015.
33. Kumar, V.; Shih, C. *Fully Plastic Crack Solutions, Estimation Scheme, and Stability Analyses for the Compact Specimen*; ASTM International: West Conshohocken, PA, USA, 1980.
34. Robert, O.R.; Dong, L. *Chapter 5—Crack-Tip Opening Displacement (CTOD)*; Elsevier: Oxford, UK, 2021; pp. 75–80.
35. Huang, Y.; Guo, F. Effect of plastic deformation on the elastic stress field near a crack tip under small-scale yielding conditions: An extended Irwin's model. *Eng. Fract. Mech.* **2021**, *254*, 107888. [[CrossRef](#)]
36. Broek, D. *Elementary Engineering Fracture Mechanics*; Springer: Dordrecht, The Netherlands, 1982.
37. Wang, Y.; Wang, W.; Zhang, B.; Li, C.-Q. A new method to determine fracture resistance curve of steel under various in-plane loading. *Eng. Fract. Mech.* **2021**, *248*, 107701. [[CrossRef](#)]
38. Lei, Z.; Bai, R.; Deng, L.; Qiu, W. Noncontact optical measurement of CTOA and CTOD for interface crack in DCB test. *Optics Lasers Eng.* **2012**, *50*, 964–970.
39. Vasco-Olmo, J.M.; Díaz, F.; Antunes, F.V.; James, M.N. Characterisation of fatigue crack growth using digital image correlation measurements of plastic CTOD. *Theor. Appl. Fract. Mech.* **2019**, *101*, 332–341. [[CrossRef](#)]
40. McClung, R. The influence of applied stress, crack length, and stress intensity factor on crack closure. *Metall. Trans. A* **1991**, *22*, 1559–1571. [[CrossRef](#)]

41. Xue, C.; He, A.; Yong, H.; Zhou, Y. Crack tip opening displacement in a linear strain hardening material. *Mech. Mater.* **2013**, *66*, 21–34. [[CrossRef](#)]
42. Xue, C.; Yong, H.; Zhou, Y. Crack tip field in a linear elastic–plastic strain-hardening material. *Int. J. Solids Struct.* **2012**, *49*, 3447–3452. [[CrossRef](#)]